

# DefVINS: Visual–Inertial Odometry for Deformable Scenes

Samuel Cerezo<sup>1</sup>, Javier Civera<sup>1</sup>

**Abstract**—Deformable scenes violate the rigidity assumptions underpinning classical visual–inertial odometry (VIO), often leading to over–fitting to local non–rigid motion or to severe camera pose drift when deformation dominates visual parallax. In this paper, we introduce DefVINS, the first visual–inertial odometry pipeline designed to operate in deformable environments. Our approach models the odometry state by decomposing it into a rigid, IMU-anchored component and a non-rigid scene warp represented by an embedded deformation graph. As a second contribution, we present VIMandala, the first benchmark containing real images and ground-truth camera poses for visual–inertial odometry in deformable scenes. In addition, we augment the synthetic Drunkard’s benchmark with simulated inertial measurements to further evaluate our pipeline under controlled conditions. We also provide an observability analysis of the visual–inertial deformable odometry problem, characterizing how inertial measurements constrain camera motion and render otherwise unobservable modes identifiable in the presence of deformation. This analysis motivates the use of IMU anchoring and leads to a conditioning-based activation strategy that avoids ill-posed updates under poor excitation. Experimental results on both in the synthetic Drunkard’s and our real VIMandala benchmarks show that DefVINS outperforms rigid visual–inertial and non-rigid visual odometry baselines. Our source code and data will be released upon acceptance.

## I. INTRODUCTION

Visual–Inertial Odometry (VIO) and SLAM are foundational technologies driving modern mobile robotics and Augmented Reality (AR). The combination of a camera with an Inertial Measurement Unit (IMU) stands out as a particularly robust sensing modality. The IMU helps handle challenging conditions such as low-texture environments and rapid motions, while making roll and pitch directly observable [1]. By providing high-frequency measurements of linear acceleration and angular velocity, the IMU effectively constrains the short-term pose dynamics and improves the observability of orientation and scale components that remain ambiguous in pure monocular vision. In turn, the camera leverages exteroceptive landmarks from the environment that constrain its six-degrees-of-freedom motion for larger temporal windows, mitigating the inevitable proprioceptive drift [2], [3]. State-of-the-art VIO systems, such as VINS-Mono [3] and OKVIS [4], have demonstrated strong performance in static, rigid environments, establishing them as a de facto standard for ego-motion estimation.

However, the efficacy of classical VIO relies fundamentally on the assumption of scene rigidity [5]. This assumption

is violated in real-world scenarios, most notably when imaging deformable objects such as human bodies or clothing. When the underlying geometric model fails to account for non-rigid motion, the performance of VIO systems deteriorates significantly. In such cases, the estimation may suffer from early over–fitting of the rigid model to local non-rigid motion, or, more severely, from substantial drift when deformation-induced parallax dominates the inter-frame motion [6]. Consequently, achieving robust and accurate localization in highly dynamic and deformable environments remains an open and critical research challenge [7].

Beyond modeling challenges, the transition from rigid to deformable environments fundamentally alters the observability properties of the estimation problem. Classical analyses of VIO observability have established that inertial sensing renders scale, gravity direction, and roll–pitch observable in rigid scenes. However, the implications of these properties in the presence of non-rigid motion remain largely unexplored. Deformation introduces additional latent degrees of freedom that may strongly couple with camera motion, leading to severe ill-conditioning and ambiguity when relying on visual information alone. In this context, inertial measurements play a crucial role by anchoring rigid-body dynamics over short time horizons, thereby constraining the solution space and reducing spurious correlations between ego-motion and non-rigid deformation. Motivated by this observation, our work presents an explicit observability analysis of the visual–inertial deformable odometry problem, showing that inertial measurements substantially improve conditioning and introduce structural constraints that are otherwise absent in purely visual formulations.

In this paper, we introduce DefVINS, the first visual–inertial odometry explicitly designed for deformable scenes. DefVINS incorporates an embedded deformation graph to model the non-rigid warping of the scene, while carefully decoupling the rigid, IMU-anchored state from the scene’s non-rigid degrees of freedom. Given the absence of benchmarks specifically targeting non-rigid VIO, we also contribute two new evaluation resources: (1) an extension of the synthetic Drunkard’s dataset augmented with inertial measurements, and (2) VIMandala, a novel real-world dataset featuring visual–inertial data and camera pose ground truth while observing a deformable mandala cloth. Experimental results on both datasets demonstrate that DefVINS consistently outperforms rigid visual–inertial methods as well as existing deformable visual odometry baselines.

<sup>1</sup>Authors are with the Departamento de Informática e Ingeniería de Sistemas, Universidad de Zaragoza, 50018 Zaragoza, ES. E-mails: {sacerezo, jcivera}@unizar.es

## II. RELATED WORK

Visual–Inertial Odometry (VIO) is a well–established paradigm for robust ego–motion estimation in rigid environments through the tight fusion of visual and inertial measurements [8], [9], [10]. Inertial sensing provides high–rate motion constraints that resolve metric scale and stabilize roll and pitch, while visual observations offer global referencing and mitigate drift. The observability and consistency properties of such systems have been studied extensively under rigid–scene assumptions, showing that scale, gravity, velocity, and IMU biases become observable only under sufficient excitation and appropriate modeling choices [11], [12], [13]. These analyses, however, fundamentally assume that all observed features belong to a single rigid body.

When this assumption is violated, visual residuals become inconsistent and may bias the estimation or lead to divergence. Several approaches address dynamic scenes, composed of several rigid objects with independent motions, by detecting and suppressing dynamic elements via semantic segmentation or motion consistency checks [14], [15], [16]. While effective under moderate dynamic content, these methods rely on rigid scene parts for camera motion estimation, which limit their applicability in scenes dominated by non–rigid motion. Other approaches are able to track dynamic content [17], [18], [19], [20] and may be more resilient to the lack of rigid scene parts. However, they also model the scene as a set of rigidly moving objects, limiting certain applications.

A complementary line of work explicitly models fully non–rigid scene geometry, targeting among others human or medical reconstruction. DynamicFusion [21], DefSLAM [22], and NR–SLAM [23] represent deformation using embedded deformation graphs or learned warp fields, enabling compelling reconstructions. However, DynamicFusion relies on RGB–D sensors, which are rarely found in some setups. And DefSLAM and NR–SLAM rely exclusively on visual cues, lack inertial anchoring, and do not preserve metric scale, resulting in a strong coupling between camera motion and scene deformation and, consequently, ill–conditioned pose estimation under strong non–rigid motion.

From a state–estimation perspective, prior work has extensively analyzed degeneracy, excitation, and observability in rigid VIO systems [11], [13], [24], [25]. In deformable environments, however, a significant portion of the observed parallax may originate from scene motion rather than camera motion, effectively reducing rigid excitation and degrading conditioning in ways not captured by existing rigid–scene analyses. To date, no prior work explicitly characterizes how inertial measurements affect the observability and conditioning of visual–inertial estimation in the presence of non–rigid deformation.

To the best of our knowledge, no existing method jointly (i) integrates an explicit deformation model within a visual–inertial odometry pipeline, and (ii) maintains a rigid, IMU–anchored reference to ensure metric consistency. DefVINS addresses these limitations by embedding a deformation

graph within a visual–inertial optimization framework and by explicitly analyzing the observability properties of the resulting system, demonstrating that inertial constraints significantly improve conditioning even under strong non–rigid motion.

## III. VISUAL–INERTIAL ODOMETRY

### A. State definition

Our state is defined over a set of  $N$  consecutive keyframes in a sliding window that we denote by their indices  $\mathcal{W} = \{\tau\}_{\tau=1}^N$ . For every keyframe at a specific time instant  $t_\tau$ ,  $\tau \in \mathcal{W}$ , we store its orientation  $\mathbf{R}_\tau \in \text{SO}(3)$ , velocity  $\mathbf{v}_\tau \in \mathbb{R}^3$  and position  $\mathbf{t}_\tau \in \mathbb{R}^3$  in a global reference frame. We consider short sequences and therefore assume constant gyroscope and accelerometer biases  $\mathbf{b}^g, \mathbf{b}^a \in \mathbb{R}^3$ . The direction of gravity is represented as  $\hat{\mathbf{g}} = \frac{\mathbf{g}}{\|\mathbf{g}\|} \in \mathbb{S}^2$ . To account for non–rigid scene dynamics, the state is augmented with  $\{\mathbf{x}_i^\tau\}_{i \in \mathcal{D}, \tau \in \mathcal{W}}$ , which collects the positions of the set  $\mathcal{D} = \{i\}_{i=1}^D$  of  $D$  deformation nodes active within  $\mathcal{W}$ . The full state stacks all these variables as a single vector

$$\boldsymbol{\xi} = \text{stack}\left(\{\mathbf{R}_\tau, \mathbf{v}_\tau, \mathbf{t}_\tau\}_{\tau \in \mathcal{W}}, \mathbf{b}^g, \mathbf{b}^a, \hat{\mathbf{g}}, \{\mathbf{x}_i^\tau\}_{i \in \mathcal{D}, \tau \in \mathcal{W}}\right) \quad (1)$$

### B. IMU preintegration and gravity residuals

The IMU kinematics between the time instants of two consecutive keyframes,  $t_\tau$  and  $t_{\tau+1}$ , are as follows

$$\mathbf{R}_{\tau+1} = \mathbf{R}_\tau \prod_{t_k \in [t_\tau, t_{\tau+1}]} \text{Exp}\left(\left(\tilde{\boldsymbol{\omega}}_k - \mathbf{b}^g - \boldsymbol{\eta}_k^{gd}\right) \Delta t\right), \quad (2)$$

$$\mathbf{v}_{\tau+1} = \mathbf{v}_\tau + \mathbf{g} \Delta T + \sum_{t_k \in [t_\tau, t_{\tau+1}]} \mathbf{R}_k (\tilde{\mathbf{a}}_k - \mathbf{b}^a - \boldsymbol{\eta}_k^{ad}) \Delta t, \quad (3)$$

$$\begin{aligned} \mathbf{t}_{\tau+1} = \mathbf{t}_\tau + \sum_{t_k \in [t_\tau, t_{\tau+1}]} \left( \mathbf{v}_k \Delta t + \frac{1}{2} \mathbf{g} \Delta t^2 \right) \\ + \sum_{t_k \in [t_\tau, t_{\tau+1}]} \frac{1}{2} \mathbf{R}_k (\tilde{\mathbf{a}}_k - \mathbf{b}^a - \boldsymbol{\eta}_k^{ad}) \Delta t^2, \end{aligned} \quad (4)$$

where  $\Delta t$  is the IMU sampling period and  $\tilde{\boldsymbol{\omega}}_k$  and  $\tilde{\mathbf{a}}_k$  correspond to the gyroscope and accelerometer readings at  $t_k \in [t_\tau, t_{\tau+1}]$ , which are affected by biases  $\mathbf{b}^g, \mathbf{b}^a$  and additive noise  $\boldsymbol{\eta}_k^{gd}, \boldsymbol{\eta}_k^{ad}$ . Between time instants  $t_\tau$  and  $t_{\tau+1}$ , the relative motion is constrained by rotation, velocity, and position residuals,

$$\mathbf{r}_{\Delta \mathbf{R}} = \text{Log}\left(\Delta \tilde{\mathbf{R}}_{\tau, \tau+1}^\top \mathbf{R}_\tau^\top \mathbf{R}_{\tau+1}\right) \quad (5)$$

$$\mathbf{r}_{\Delta \mathbf{v}} = \mathbf{R}_\tau^\top (\mathbf{v}_{\tau+1} - \mathbf{v}_\tau - \mathbf{g} \Delta T) - \Delta \tilde{\mathbf{v}}_{\tau, \tau+1} \quad (6)$$

$$\mathbf{r}_{\Delta \mathbf{t}} = \mathbf{R}_\tau^\top (\mathbf{t}_{\tau+1} - \mathbf{t}_\tau - \mathbf{v}_\tau \Delta T - \frac{1}{2} \mathbf{g} \Delta T^2) - \Delta \tilde{\mathbf{t}}_{\tau, \tau+1} \quad (7)$$

where  $\Delta \tilde{\mathbf{R}}_{\tau, \tau+1}$ ,  $\Delta \tilde{\mathbf{v}}_{\tau, \tau+1}$  and  $\Delta \tilde{\mathbf{t}}_{\tau, \tau+1}$  are preintegrated values from the IMU readings [26]. Each of them is weighted by its corresponding covariance matrix  $\boldsymbol{\Sigma}_{\Delta \phi}$ ,  $\boldsymbol{\Sigma}_{\Delta \mathbf{v}}$  and  $\boldsymbol{\Sigma}_{\Delta \mathbf{t}}$  obtained during the preintegration process as described in [27], Sec. III–A. Additionally, a gravity residual is introduced to enforce consistency between the estimated accelerations and the gravity direction,

$$\mathbf{r}_{\mathbf{g}} = \left( \frac{\mathbf{v}_{\tau+1} - \mathbf{v}_\tau}{\Delta T} - \frac{\mathbf{R}_\tau \Delta \mathbf{v}_{\tau, \tau+1}}{\Delta T} \right) - \|\mathbf{g}\| \hat{\mathbf{g}}, \quad (8)$$

where  $\hat{\mathbf{g}} \in \mathbb{S}^2$  and  $\|\hat{\mathbf{g}}\| = 9.81 \text{ m/s}^2$ . The contribution of the aforementioned residuals to the overall cost function is then defined as

$$\mathcal{L}_{\text{imu}}^\tau = \|\mathbf{r}_{\Delta R}\|_{\Sigma_{\Delta\phi}} + \|\mathbf{r}_{\Delta v}\|_{\Sigma_{\Delta v}} + \|\mathbf{r}_{\Delta t}\|_{\Sigma_{\Delta t}} + \|\mathbf{r}_{\mathbf{g}}\|_{\Sigma_{\mathbf{g}}} \quad (9)$$

### C. Reprojection error

Each tracked feature will contribute with its reprojection error, that will be aggregated for the keyframe at time  $t_\tau$  as

$$\mathcal{L}_{\text{rep}}^\tau = \sum_{i \in \mathcal{P}} \|\mathbf{z}_i^\tau - \pi(\mathbf{R}_\tau, \mathbf{t}_\tau, \mathbf{x}_i^\tau)\|_{\Sigma_i^\tau}, \quad (10)$$

where  $\mathbf{z}_i^\tau \in \Omega$ ,  $\Omega$  being the image domain, denotes the image measurement of the point feature  $\mathbf{x}_i^\tau \in \mathbb{R}^3$  at time  $t_\tau$ ,  $\Sigma_i^\tau$  is its associated covariance [28] and  $\pi(\cdot)$  the camera projection model. We will denote as  $\mathcal{P} = \{i\}_{i=1}^M$  the full set of 3D points tracked. Note that, differently from rigid visual-inertial odometry, the 3D scene points  $\mathbf{x}_i^\tau$  may change their position at each temporal instant  $\tau$ .

### D. Non-rigid residual

We will assume that our imaged scenes may exhibit non-rigid motions, such as those exhibited by deformable clothes or cables under physical interaction. We will model these effects by a lightweight deformation graph that we build over a subset  $\mathcal{D} = \{i\}_{i=1}^D \subset \mathcal{P}$  composed by the  $D$  longer feature tracks from  $\mathcal{P}$ . The tracked points  $\mathbf{x}_i^\tau$  define the nodes of the graph. We will define the reference keyframe as the first one at  $\tau = 1$ . Two nodes  $i, j \in \mathcal{D}$  are connected by an edge  $(i, j)$  if their distance in the reference keyframe is below a spatial threshold. This provides a compact neighborhood structure that encodes how nearby points of the scene relate to each other. The reference distance between nodes is defined in the reference keyframe as

$$d_{ij}^1 = \|\mathbf{x}_i^1 - \mathbf{x}_j^1\|. \quad (11)$$

The full non-rigid residual is built up by several terms that we detail next.

**Elastic constraint.** We will assume an elastic relation between points in the deformation graph, preventing unrealistic stretching or compression. If part of the deformable object bends, nearby nodes may also experience non-rigid deformation, but their spacing should not deviate excessively from the reference configuration. We promote this behavior by penalizing changes in pairwise distances.

$$\mathcal{L}_{ij,\text{elas}}^\tau = \kappa \frac{(d_{ij}^\tau - d_{ij}^1)^2}{d_{ij}^1}, \quad d_{ij}^\tau = \|\mathbf{x}_i^\tau - \mathbf{x}_j^\tau\|. \quad (12)$$

where  $\kappa$  is an elastic deformation constant. In words, this term will penalize excessive stretching or compression, so small deformations will be preferred for the same IMU and multi-view constraints.

**Viscous constraint.** While the elastic term controls shape deviations between times  $t_\tau$  and  $t_1$ , we additionally impose constraints on the kinematics via a viscous term. Let  $\mathbf{s}_i^\tau = \mathbf{x}_i^\tau - \mathbf{x}_i^{\tau-1}$  be the displacement of node  $i$  between two

consecutive keyframes. Following [29], we encourage nearby nodes to move in a similar manner

$$\mathcal{L}_{ij,\text{visc}}^\tau = b_{ij} \|\mathbf{s}_i^\tau - \mathbf{s}_j^\tau\|^2, \quad (13)$$

where proximity is encoded by spatially decaying weights  $b_{ij}$ , which impose strong temporal coupling between spatially close frames, promoting smooth and coherent deformations

$$b_{ij} = \exp\left(-\frac{\|\mathbf{x}_i^1 - \mathbf{x}_j^1\|^2}{2\sigma^2}\right), \quad (14)$$

being  $\sigma$  a constant modeling the strength of the viscous constraint.

**Photometric constraint.** In addition to geometric reprojection error, we also leverage image intensity information. A semi-direct strategy is adopted, in which photometric data association is carried out on Shi–Tomasi features using the modified multi-scale Lucas–Kanade tracker introduced in [30]. For every deformation node, its image projections in consecutive keyframes  $\tau-1$  and  $\tau$  are expected to correspond to pixels with similar intensities, following the classical brightness constancy assumption:

$$\mathcal{L}_{i,\text{photo}}^\tau = \left(I^\tau(\mathbf{u}_i^\tau) - \alpha_i I^{\tau-1}(\mathbf{u}_i^{\tau-1}) + \beta_i\right)^2, \quad (15)$$

where  $\mathbf{u}_i^\tau = \pi(\mathbf{R}_\tau, \mathbf{t}_\tau, \mathbf{x}_i^\tau)$  and  $I^\tau(\mathbf{u}_i)$  is evaluated via bilinear sampling. Also a local illumination invariance is achieved by computing local gain  $\alpha_i$  and bias  $\beta_i$  terms for each tracked image point. This term encourages nodes to move consistently with the apparent texture motion in the images.

The combination of the elastic, viscous and photometric terms yields the full non-rigid residual for a keyframe pair  $(\tau-1, \tau)$ :

$$\mathcal{L}_{\text{nr}}^\tau = \sum_{(i,j) \in \mathcal{E}} \left(\mathcal{L}_{ij,\text{elas}}^\tau + \mathcal{L}_{ij,\text{visc}}^\tau\right) + \sum_{i \in \mathcal{D}} \mathcal{L}_{i,\text{photo}}^\tau \quad (16)$$

where  $\mathcal{E}$  is the set of all edges in the deformation graph.

### E. Overall cost function

The visual–inertial estimation problem is formulated as a nonlinear least-squares optimization over a fixed-size sliding window  $\mathcal{W}$ . The window contains the most recent  $N$  keyframes and defines the state vector  $\xi$  over which constraints are applied. Within  $\mathcal{W}$ , our optimization jointly optimizes rigid-body motion, inertial parameters and non-rigid deformation variables as defined in Eq. 1.

As the window slides, new keyframes are added and the oldest ones are removed by marginalizing their corresponding states. This marginalization step condenses past information into a compact prior term  $\mathcal{L}_{\text{prior}}$ , which preserves some degree of consistency while keeping the computational complexity bounded. The resulting objective function minimized by the system is given by

$$\mathcal{L} = \sum_{\tau \in \mathcal{W}} \left(\mathcal{L}_{\text{imu}}^\tau + \mathcal{L}_{\text{rep}}^\tau + \lambda_{\text{nr}} \mathcal{L}_{\text{nr}}^\tau\right) + \mathcal{L}_{\text{prior}}, \quad (17)$$

where the scalar  $\lambda_{\text{nr}}$  balances the non-rigid regularization against visual and inertial terms.

$$\mathcal{O} = \begin{bmatrix} -\mathbf{J}_r^{-1}(\phi)\mathbf{R}_{\tau+1}^\top\mathbf{R}_\tau & \mathbf{0} & \mathbf{0} & \mathbf{J}_r^{-1}(\phi) & \mathbf{0} & \mathbf{0} & \mathbf{0} & \mathbf{0} & \mathbf{0} & \mathbf{0} \\ \left(\mathbf{R}_\tau^\top(\mathbf{v}_{\tau+1} - \mathbf{v}_\tau - \mathbf{g}\Delta T)\right)^\wedge & -\mathbf{R}_\tau^\top & \mathbf{0} & \mathbf{0} & \mathbf{R}_\tau^\top & \mathbf{0} & \mathbf{0} & -\mathbf{R}_\tau^\top\Delta T & -\|\mathbf{g}\|\mathbf{R}_\tau^\top\Delta T & \mathbf{0} \\ \left(\mathbf{R}_\tau^\top(\mathbf{t}_{\tau+1} - \mathbf{t}_\tau - \mathbf{v}_\tau\Delta T - \frac{1}{2}\mathbf{g}\Delta T^2)\right)^\wedge & -\mathbf{R}_\tau^\top\Delta T & -\mathbf{R}_\tau^\top & \mathbf{0} & \mathbf{0} & \mathbf{R}_\tau^\top & \mathbf{0} & -\mathbf{R}_\tau^\top\frac{1}{2}\Delta T^2 & -\frac{1}{2}\|\mathbf{g}\|\mathbf{R}_\tau^\top\Delta T^2 & \mathbf{0} \\ \mathbf{H}_{\mathbf{R}_\tau}^{\text{vis}} & \mathbf{0} & \mathbf{H}_{\mathbf{t}_\tau}^{\text{vis}} & \mathbf{H}_{\mathbf{R}_{\tau+1}}^{\text{vis}} & \mathbf{0} & \mathbf{H}_{\mathbf{t}_{\tau+1}}^{\text{vis}} & \mathbf{0} & \mathbf{0} & \mathbf{0} & \mathbf{H}_{\text{nr}}^{\text{vis}} \\ \mathbf{0} & \mathbf{H}_{\text{nr}}^{\text{elas}} \\ \mathbf{0} & \mathbf{H}_{\text{nr}}^{\text{visc}} \\ \mathbf{H}_{\mathbf{R}_\tau}^{\text{photo}} & \mathbf{0} & \mathbf{H}_{\mathbf{t}_\tau}^{\text{photo}} & \mathbf{H}_{\mathbf{R}_{\tau+1}}^{\text{photo}} & \mathbf{0} & \mathbf{H}_{\mathbf{t}_{\tau+1}}^{\text{photo}} & \mathbf{0} & \mathbf{0} & \mathbf{0} & \mathbf{H}_{\text{nr}}^{\text{photo}} \\ \mathbf{0} & \mathbf{0} & \mathbf{0} & \mathbf{0} & \mathbf{0} & \mathbf{0} & \mathbf{I}_3 & \mathbf{0} & \mathbf{0} & \mathbf{0} \\ \mathbf{0} & \mathbf{I}_3 & \mathbf{0} & \mathbf{0} \\ \mathbf{0} & -\frac{1}{\Delta T}\mathbf{I}_3 & \mathbf{0} & \mathbf{0} & \frac{1}{\Delta T}\mathbf{I}_3 & \mathbf{0} & \mathbf{0} & \mathbf{0} & -\|\mathbf{g}\|\mathbf{J}_{\mathbf{g}2} & \mathbf{0} \end{bmatrix}$$

Fig. 1: **Structure of the full observability matrix**  $\mathcal{O}$ . The matrix explicitly incorporates the accelerometer bias into the state. Each block row corresponds to the Jacobians of the different measurement and constraint terms, including IMU preintegration factors, visual residuals, non-rigid motion priors, and bias and gravity constraints. This structured formulation highlights the contribution of each sensing modality to the overall system observability.

### F. Observability analysis

Following [27], observability is assessed from a discrete-time perspective by linearizing the measurement residuals over a finite temporal window. Although Lie derivatives are not explicitly computed, the resulting Jacobians capture the local sensitivity of the residuals with respect to the state, analogously to the continuous-time formulation. As shown in [31], [13], the rank of the stacked Jacobian matrix determines the locally observable directions and is critical for estimator consistency.

Within this framework, we analyze observability over a two-keyframe window  $\{\tau-1, \tau\}$ , jointly considering inertial preintegration, geometric visual, and non-rigid deformation residuals acting on the state (1). The corresponding observability matrix  $\mathcal{O}$  is obtained by stacking the Jacobians of all residuals with respect to the state vector  $\xi$ , yielding

$$\mathcal{O} = \begin{bmatrix} \frac{\partial \mathbf{r}_{\Delta R}^\tau}{\partial \xi}^\top, \frac{\partial \mathbf{r}_{\Delta v}^\tau}{\partial \xi}^\top, \frac{\partial \mathbf{r}_{\Delta t}^\tau}{\partial \xi}^\top, \frac{\partial \mathbf{r}_{\text{rep}}^\tau}{\partial \xi}^\top, \frac{\partial \mathbf{r}_{\text{elas}}^\tau}{\partial \xi}^\top, \\ \frac{\partial \mathbf{r}_{\text{visc}}^\tau}{\partial \xi}^\top, \frac{\partial \mathbf{r}_{\text{photo}}^\tau}{\partial \xi}^\top, \frac{\partial \mathbf{r}_{\text{bg}}^\tau}{\partial \xi}^\top, \frac{\partial \mathbf{r}_{\text{ba}}^\tau}{\partial \xi}^\top, \frac{\partial \mathbf{r}_{\text{g}}^\tau}{\partial \xi}^\top \end{bmatrix}. \quad (18)$$

Based on the previously defined residuals, Fig. 1 illustrates the explicit block structure of the observability matrix  $\mathcal{O}$ . For clarity and readability, the analytical expressions of the nonzero Jacobian blocks are reported in the text rather than embedded in the figure. Geometric reprojection residuals contribute with standard visual-inertial Jacobian blocks, namely  $\mathbf{H}_{\mathbf{R}_\tau}^{\text{vis}} = -\mathbf{J}_\pi \mathbf{t}_{\text{cam}}^\wedge$ ,  $\mathbf{H}_{\mathbf{t}_\tau}^{\text{vis}} = -\mathbf{J}_\pi \mathbf{R}_\tau^\top$ , and  $\mathbf{H}_{\text{nr}}^{\text{vis}} = \mathbf{J}_\pi \mathbf{R}_\tau^\top$  for the deformation nodes. Non-rigid regularization terms introduce additional couplings among deformation variables: the elastic prior yields  $\mathbf{H}_{\text{nr}}^{\text{elas}} \propto (\mathbf{x}_j^\tau - \mathbf{x}_j^\tau)/d_{ij}^\tau$ , the viscous term results in block structures of the form  $[\mathbf{I}, -\mathbf{I}, -\mathbf{I}, \mathbf{I}]$ , and the photometric term contributes  $\mathbf{H}_{\text{nr}}^{\text{photo}} = \nabla I^\tau(\mathbf{u}_i^\tau) \mathbf{J}_\pi \mathbf{R}_\tau^\top$ , with analogous derivatives with respect to the pose variables. Together, these expressions define all nonzero blocks of  $\mathcal{O}$ .

A symbolic inspection of the resulting Jacobian structure shows that the formulation preserves the classical gauge

freedoms of visual-inertial odometry while introducing additional degrees of freedom associated with the non-rigid deformation field. When the non-rigid variables  $\{\mathbf{x}_i^\tau\}_{i \in \mathcal{D}, \tau \in \mathcal{W}}$  are ignored and metric depth is assumed, the rigid subsystem remains observable only up to a global  $SE(3)$  transformation: absolute position and yaw are unobservable, whereas gravity magnitude and direction become observable under sufficiently rich accelerations and rotations [31]. In particular, the IMU velocity and position residuals  $\mathbf{r}_{\Delta v}^\tau$  and  $\mathbf{r}_{\Delta t}^\tau$  couple accelerometer bias and gravity, becoming rank-deficient under near-constant-velocity motion, while insufficient rotational excitation leaves yaw and gyroscope bias coupled in  $\mathbf{r}_{\Delta R}^\tau$ .

The non-rigid substate is constrained by the combined action of geometric reprojection, photometric consistency, and visco-elastic regularization. Visual and photometric terms anchor node motion to image evidence, whereas elastic and viscous priors regularize spatial and temporal variations, eliminating low-energy deformation modes that would otherwise be consistent with visual measurements alone. As a result, the rank of  $\mathcal{O}$  increases in the non-rigid subspace.

Although inertial measurements do not directly observe the deformation field, they improve its observability indirectly by stabilizing the global rigid trajectory. Once gravity and inertial biases are sufficiently well conditioned, deformation nodes can no longer absorb errors in global pose or yaw, reducing their ability to mimic rigid drift. Consequently, sufficiently rich inertial excitation helps decouple rigid motion from non-rigid deformation and further constrains the remaining deformation modes.

In practice, the rank of  $\mathcal{O}$  depends on both motion and deformation patterns. Trajectories with limited parallax or negligible rotation lead to weak observability of inertial quantities and non-rigid modes, whereas well-excited motions combined with visco-elastic regularization yield a well-conditioned system in which the rigid state is observable up to the expected gauge freedoms and the deformation field is sufficiently constrained.

TABLE I: **Drunkard’s Dataset results.** We report ATE RMSE, RPE, and number of successfully tracked frames. Each row averages all scenes at the same deformation level. Best result per metric in **bold**. Last row shows per-column means.

Seq.	Deformation	ATE RMSE [mm]						RPE [mm]						#Frames							
		ORB-SLAM3		NR-SLAM		DefVINS		ORB-SLAM3		NR-SLAM		DefVINS		ORB-SLAM3		NR-SLAM		DefVINS			
				V-NR	VI-R	Full			V-NR	VI-R	Full			V-NR	VI-R	Full			V-NR	VI-R	Full
L0	Low	6.0	<b>5.4</b>	9.2	7.1	6.8	1.1	<b>1.0</b>	2.2	1.9	1.2	1987	2061	2124	2169	<b>2198</b>					
L1	Medium	19.4	11.6	17.1	13.2	<b>9.4</b>	2.1	2.0	3.1	2.4	<b>2.0</b>	1879	1968	2057	2096	<b>2128</b>					
L2	Hard	42.3	19.5	27.4	21.1	<b>14.3</b>	3.2	<b>3.0</b>	4.1	3.4	3.1	1746	1842	1928	1986	<b>2021</b>					
L3	Extreme	53.1	25.4	39.2	30.3	<b>19.6</b>	5.0	4.3	5.2	4.1	<b>3.3</b>	1612	1729	1814	1876	<b>1919</b>					
Mean		30.2	15.5	23.2	17.9	<b>12.5</b>	2.85	2.6	3.7	3.0	<b>2.4</b>	1806	1900	1981	2032	<b>2067</b>					

#### IV. EXPERIMENTS

All experiments were conducted on a desktop PC with an Intel Core i7-11700K (3.6 GHz, 64 GB RAM). The proposed method is implemented in C++ and uses Ceres<sup>1</sup> for optimization purposes. Unless otherwise stated, all methods run in a single thread and wall-clock times are reported. Performance is evaluated using standard trajectory-based metrics. We report Absolute Trajectory Error (ATE), Relative Position Error (RPE), and the number of successfully tracked frames as an indicator of robustness. Comparisons are performed against ORB-SLAM3 [10] as a rigid visual-inertial SLAM baseline and NR-SLAM [23] as a non-rigid visual alternative. We first evaluate the method on the Drunkard’s Dataset [32], which provides 19 synthetic sequences (320×320) with full 3D ground truth and four increasing deformation levels per scene, enabling controlled analysis. We then further validate DefVINS on our VIMandala dataset, comprising seven 848×480 real sequences for which synchronized RGB, depth IMU, and ground-truth camera motion are recorded. The sequences, that we denote as R0–R6, capture progressively stronger non-rigid deformations of a textured mandala cloth.

##### A. Synthetic experiments in the Drunkard’s dataset

To evaluate the robustness of DefVINS under controlled conditions, we evaluate it on the Drunkard’s Dataset. This dataset consists of synthetic RGB-D sequences exhibiting progressively increasing levels of non-rigid deformation, ranging from near-rigid motion to large-amplitude surface dynamics. As inertial measurements are not provided, IMU data are synthetically generated by differentiating ground-truth trajectories represented as B-splines, ensuring temporally smooth and physically consistent signals.

Table I reports quantitative results on Drunkard’s, which comprises 19 synthetic scenes evaluated at four increasing levels of deformation difficulty. Results are averaged across scenes at each deformation level to provide compact yet representative metrics. For our DefVINS, we report results for the full pipeline, but also for the ablated versions V-NR (no inertial measurements) and VI-R (rigid scene model).

In low-deformation scenarios (L0), all methods achieve similarly low errors. In this regime, the rigid visual–inertial baseline ORB-SLAM3 performs competitively against non-rigid approaches, indicating that explicit non-rigid modeling

is not strictly necessary when deformations are minimal. Nevertheless, the incorporation of inertial measurements already provides measurable benefits: compared to the visual-only DefVINS configuration (V-NR), the rigid visual–inertial variant (VI-R) reduces ATE by roughly 20%. As deformation increases to moderate levels (L1), performance differences become more pronounced. While ORB-SLAM3 exhibits a substantial increase in ATE relative to L0, both NR-SLAM and DefVINS maintain significantly lower errors. In particular, our full DefVINS formulation achieves an ATE reduction of approximately 30% with respect to ORB-SLAM3 and nearly 45% compared to the visual-only baseline.

Improvements in RPE remain more moderate (around 20–30%), suggesting that inertial constraints primarily contribute to stabilizing short-term motion estimates. In harder deformation regimes (L2), rigid motion assumptions further degrade estimation accuracy. Relative to ORB-SLAM3, the full DefVINS formulation reduces ATE by approximately 35–40% and RPE by about 25%. Moreover, when compared to the rigid DefVINS variant (VI-R), the inclusion of explicit non-rigid regularization yields an additional ATE reduction of roughly 30%, highlighting the importance of modeling deformation dynamics beyond inertial stabilization alone. In the extreme deformation case (L3), the limitations of rigid models become most evident. The full DefVINS formulation achieves an ATE reduction of approximately 40–45% with respect to ORB-SLAM3 and nearly 50% compared to the visual-only configuration, while also reducing RPE by about 40%. Although all methods experience a reduction in the number of successfully tracked frames as deformation severity increases, DefVINS consistently achieves the longest estimated trajectories, indicating improved robustness to severe non-rigid motion.

Overall, results on the Drunkard’s Dataset confirm that inertial sensing and explicit non-rigid regularization provide complementary benefits. While inertial constraints primarily improve local motion consistency, non-rigid modeling is essential to recover globally accurate trajectories as deformation amplitude increases, even under idealized synthetic conditions.

##### B. Observability analysis

To complement the quantitative evaluation, we present an illustrative analysis of numerical conditioning under controlled synthetic conditions. A set of short motion segments

<sup>1</sup><http://ceres-solver.org/>

TABLE II: **Comparison of visual–inertial odometry methods on the VIMandala dataset.** We report ATE RMSE, RPE, and number of successfully tracked frames. Best result per metric in **bold**. Last row shows per-column means.

Seq.	Deformation	ATE RMSE [mm]					RPE [mm]					#Frames				
		ORB-SLAM3	NR-SLAM	DefVINS			ORB-SLAM3	NR-SLAM	DefVINS			ORB-SLAM3	NR-SLAM	DefVINS		
				V-NR	VI-R	Full			V-NR	VI-R	Full			V-NR	VI-R	Full
R0	Low	<b>6.9</b>	7.1	10.8	8.9	8.1	<b>1.2</b>	1.4	1.9	1.6	1.5	<b>1810</b>	1804	1805	1802	1804
R1	Low	<b>7.5</b>	8.6	13.2	10.6	9.0	<b>1.4</b>	1.6	2.1	1.8	1.6	1684	1743	1751	1743	<b>1770</b>
R2	Medium	15.3	10.5	19.6	15.1	<b>10.2</b>	2.3	2.2	2.7	2.5	<b>2.0</b>	1589	1658	1706	1742	<b>1768</b>
R3	Medium	27.6	17.9	26.4	19.9	<b>10.8</b>	3.5	3.0	3.1	2.5	<b>2.1</b>	1496	1592	1651	1688	<b>1719</b>
R4	Medium	48.1	19.4	30.8	24.9	<b>11.4</b>	4.6	3.4	3.1	2.0	<b>1.9</b>	1387	1504	1568	1603	<b>1736</b>
R5	High	71.4	39.8	44.5	33.2	<b>15.6</b>	6.1	4.5	4.0	2.9	<b>2.4</b>	1194	1542	1623	1668	<b>1706</b>
R6	High	95.8	57.2	60.8	41.0	<b>19.8</b>	7.8	5.2	4.7	3.5	<b>3.0</b>	982	1476	1558	1604	<b>1641</b>
Mean		39.0	22.9	29.4	22.0	<b>12.1</b>	3.84	3.04	3.09	2.40	<b>2.07</b>	1449	1617	1666	1693	<b>1735</b>

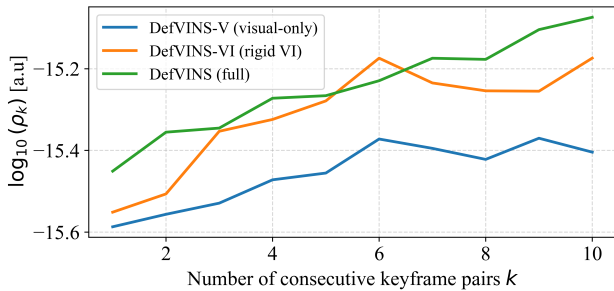


Fig. 2: **Illustrative observability analysis under synthetic conditions.** Evolution of the conditioning score  $\log_{10}(\rho_k)$  as a function of the number of stacked keyframe pairs  $k$ . Inertial sensing and non-rigid regularization significantly improve numerical conditioning, yielding well-observed directions with only a few frames.

with rich 6-DoF excitation is selected from the synthetic dataset. Specifically, we extract five non-overlapping segments of ten consecutive keyframes each, characterized by non-collinear translations and rotations about multiple axes. For each segment, residual Jacobians are generated and stacked over  $k$  consecutive keyframe pairs to form the observability matrix  $\mathcal{O}$ . The reported results correspond to the average conditioning score across the selected segments. Numerical observability is quantified using the conditioning score  $\rho_k = \sigma_{\min}/\sigma_{\max}$ , where  $\sigma_{\min}$  and  $\sigma_{\max}$  denote the smallest and largest singular values of  $\mathcal{O}$ , respectively. Fig. 2 shows  $\log_{10}(\rho_k)$  as a function of the number of stacked keyframe pairs for the visual-only, rigid visual–inertial, and full formulations. The numerical conditioning evolves very differently for the aforementioned configurations. Inertial constraints lift near-null modes associated with gravity and biases, and non-rigid regularization prevents deformation variables from absorbing rigid-body drift. As a result, the full formulation becomes well conditioned with only a few frames, explaining the improved robustness observed in the synthetic experiments.

### C. Real experiments in the VIMandala dataset

The synthetic evaluation is complemented with a set of realistic experiments aimed at assessing the behavior of the proposed non-rigid regularization under natural image noise, real sensor motion, and uncontrolled surface deformations. To this end, we present the VIMandala dataset composed of seven RGB-D sequences, each of them captured on a textured deformable surface and exhibiting a different degree of non-rigid motion. The sequences are denoted as R0–R6, where R0 corresponds to near-rigid motion and R6 represents the most severe deformations. This gradual increase in deformation enables a systematic evaluation of the stability of the proposed visco–elastic prior under progressively more challenging conditions. Table II summarizes the quantitative performance of all evaluated methods on the real deformable sequences R0–R6. Several consistent trends can be observed across deformation regimes.

For the nearly rigid sequences (R0–R1), the rigid visual–inertial baseline ORB-SLAM3 achieves the lowest ATE and RPE values, outperforming the deformable models by approximately 20–30% in ATE. This confirms that classical rigid visual–inertial approaches remain highly effective when surface deformation is negligible, and we attribute these better results to the better engineered implementation of ORB-SLAM3. In this regime, all DefVINS variants are able to track almost the full sequence length, with only marginal accuracy degradation. As the degree of deformation increases to moderate levels (R2–R3), rigid assumptions progressively break down. Although ORB-SLAM3 and NR-SLAM still maintain tracking, both exhibit a marked increase in ATE. In contrast, incorporating inertial measurements within the DefVINS framework (VI-R) reduces ATE by approximately 25–30% with respect to the visual-only configuration (V-NR), while also lowering RPE by around 15–20%. This highlights the stabilizing effect of inertial constraints on rotational estimation and short-term motion consistency. NR-SLAM consistently achieves intermediate performance, outperforming the rigid ORB-SLAM3 but still falling short of our proposed DefVINS. For medium-to-high deformation scenarios (R4–R6), the limitations of rigid scene models become evident. Relative to ORB-SLAM3, the full DefVINS formulation reduces ATE by approximately 75% on R4, around 80% on

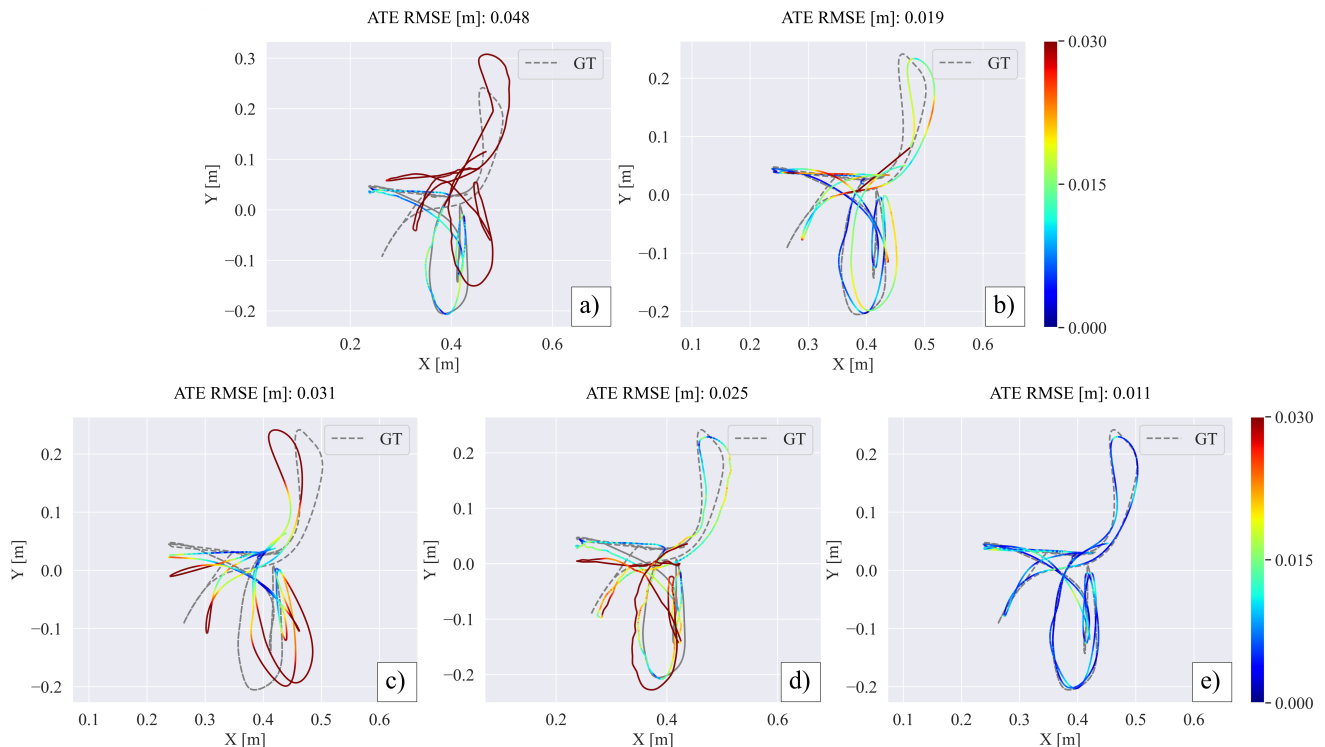


Fig. 3: **Comparison between DefVINS operating modes and baselines in R4 sequence.** a) **ORB-SLAM3**: a representative rigid visual-inertial system. b) **NR-SLAM**: a representative non-rigid visual SLAM pipeline, with focus on medical applications. c) **DefVINS-V** (visual-only, non-rigid): the lack of inertial constraints leads to accumulated drift, particularly during turning motions. b) **DefVINS-VI** (rigid): introducing inertial sensing stabilizes rotational estimates, but assuming scene rigidity limits performance under deformation. e) **DefVINS (full)**: by jointly enabling inertial sensing and explicit non-rigid modeling, DefVINS achieves the global consistency and lowest trajectory error. Dashed line represent the ground-truth while colored line represent the camera trajectory and its estimation errors.

R5, and close to 80% on R6. At the same time, DefVINS (Full) consistently tracks a substantially larger fraction of frames (around 85–95%) compared to ORB-SLAM3, whose tracking coverage drops below 50% in R4 and below 20% in R6. While inertial sensing alone partially mitigates tracking degradation, only the joint combination of inertial constraints and explicit non-rigid regularization preserves both accuracy and robustness under strong deformation.

Overall, these results demonstrate that inertial sensing and non-rigid modeling play complementary roles. Inertial measurements primarily stabilize local motion and reduce short-term drift, whereas explicit non-rigid regularization is essential to maintain global consistency and long-term tracking in highly deformable environments.

To assess the contribution of each system component, the proposed framework is evaluated under multiple operating modes obtained by selectively enabling inertial sensing and non-rigid modeling. Fig. 3 qualitatively compares the resulting camera trajectories for a visual-only configuration (DefVINS-V), a rigid visual-inertial setup without non-rigid regularization (DefVINS-VI), and the full DefVINS model, which jointly exploits inertial constraints and non-rigid motion modeling. Results are also compared against ORB-SLAM3 and NR-SLAM. This ablation study highlights

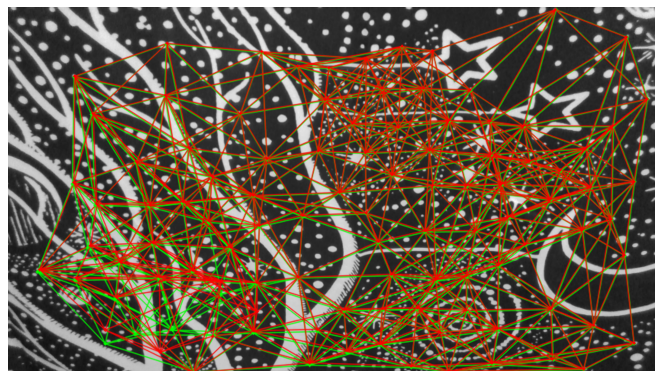


Fig. 4: **Deformation graph on sequence R4.** Green and red edges denote the graph at times  $t-1$  and  $t$ , respectively. Their differences indicate medium-to-high non-rigid deformation, with stronger effects in the lower-left region.

the complementary roles of inertial sensing and non-rigid regularization, and exposes the limitations of rigid motion assumptions in deformable scenes.

To illustrate the estimated surface behavior, Fig. 4 shows the deformation graph for a representative image of our VIMandala dataset. The graph reveals spatially varying de-

formation, with larger displacements in the lower-left region and comparatively stable behavior elsewhere, demonstrating the ability of the proposed visco-elastic regularization to capture localized deformations while maintaining global surface coherence.

## V. CONCLUSIONS

This paper introduced DefVINS, a visual-inertial odometry pipeline for deformable scenes that decouples a rigid, IMU-anchored state from progressively activated non-rigid deformation parameters. In addition, given the lack of benchmarks for this task, we contribute by synthesizing IMU readings for the synthetic Drunkard’s dataset and curating a new real benchmark imaging a deforming mandala. Our experiments on both synthetic and real data demonstrate that our DefVINS provides accurate and stable state estimation across a wide range of deformation regimes, outperforming relevant rigid visual-inertial and non-rigid visual baselines.

## REFERENCES

- [1] G. P. Huang, “Visual-inertial navigation: A concise review,” *2019 International Conference on Robotics and Automation (ICRA)*, pp. 9572–9582, 2019.
- [2] V. Usenko, J. Engel, J. Stückler, and D. Cremers, “Direct visual-inertial odometry with stereo cameras,” in *2016 IEEE international conference on robotics and automation (ICRA)*. IEEE, 2016, pp. 1885–1892.
- [3] T. Qin, P. Li, and S. Shen, “Vins-mono: A robust and versatile monocular visual-inertial state estimator,” *IEEE Transactions on Robotics*, vol. 34, no. 4, pp. 1004–1020, 2018.
- [4] S. Leutenegger, S. Lynen, M. Bosse, R. Siegwart, and P. Furgale, “Keyframe-based visual-inertial odometry using nonlinear optimization,” *The International Journal of Robotics Research*, vol. 34, no. 3, pp. 314–334, 2015.
- [5] F. Dellaert and M. Kaess, “Factor graphs for robot perception,” *Foundations and Trends in Robotics*, vol. 6, pp. 1–139, 01 2017.
- [6] R. A. Newcombe, S. Izadi, O. Hilliges, D. Molyneaux, D. Kim, A. J. Davison, P. Kohi, J. Shotton, S. Hodges, and A. Fitzgibbon, “Kinectfusion: Real-time dense surface mapping and tracking,” in *2011 10th IEEE international symposium on mixed and augmented reality*. Ieee, 2011, pp. 127–136.
- [7] J. Zhu, A. Cherubini, C. Dune, D. Navarro-Alarcon, F. Alambeigi, D. Berenson, F. Ficuciello, K. Harada, J. Kober, X. Li, J. Pan, W. Yuan, and M. Gienger, “Challenges and outlook in robotic manipulation of deformable objects,” *IEEE Robotics and Automation Magazine*, vol. 29, no. 3, pp. 67–77, 2022.
- [8] S. Leutenegger, S. Lynen, M. Bosse, R. Siegwart, and P. Furgale, “Keyframe-based visual-inertial odometry using nonlinear optimization,” *The International Journal of Robotics Research*, vol. 34, no. 3, pp. 314–334, 2015.
- [9] T. Qin, P. Li, and S. Shen, “Vins-mono: A robust and versatile monocular visual-inertial state estimator,” in *IEEE International Conference on Robotics and Automation (ICRA)*, 2018, pp. 1–7.
- [10] C. Campos, R. Elvira, J. J. G. Rodríguez, J. M. Montiel, and J. D. Tardós, “Orb-slam3: An accurate open-source library for visual, visual-inertial, and multimap slam,” *IEEE transactions on robotics*, vol. 37, no. 6, pp. 1874–1890, 2021.
- [11] J. Hesch, F. Mirzaei, G.-L. Mariottini, and S. Roumeliotis, “Cameraimu alignment from closed-form solutions,” *IEEE Transactions on Robotics*, vol. 30, no. 5, pp. 1058–1067, 2014.
- [12] A. Martinelli, “Closed-form solution of visual-inertial structure from motion,” in *IEEE International Conference on Robotics and Automation (ICRA)*, 2013, pp. 5214–5221.
- [13] G. P. Huang, A. I. Mourikis, and S. I. Roumeliotis, “Observability-based rules for designing consistent ekf slam estimators,” in *IEEE International Conference on Robotics and Automation (ICRA)*. IEEE, 2009, pp. 3871–3877.
- [14] B. Bescós, J. M. Fàcil, J. Civera, and J. Neira, “DynaSLAM: Tracking, mapping, and inpainting in dynamic scenes,” *IEEE Robotics and Automation Letters (RA-L)*, vol. 3, no. 4, pp. 4076–4083, 2018.
- [15] S. Song, H. Lim, A. J. Lee, and H. Myung, “Dynavins: A visual-inertial slam for dynamic environments,” *IEEE Robotics and Automation Letters*, vol. 7, no. 4, pp. 11 523–11 530, 2022.
- [16] —, “Dynavins++: Robust visual-inertial state estimator in dynamic environments by adaptive truncated least squares and stable state recovery,” *IEEE Robotics and Automation Letters*, 2024.
- [17] I. Ballester, A. Fontán, J. Civera, K. H. Strobl, and R. Triebel, “Dot: Dynamic object tracking for visual slam,” in *2021 IEEE international conference on robotics and automation (ICRA)*. IEEE, 2021, pp. 11 705–11 711.
- [18] B. Bescos, C. Campos, J. D. Tardos, and J. Neira, “DynaSLAM ii: Tightly-coupled multi-object tracking and slam,” *IEEE robotics and automation letters*, vol. 6, no. 3, pp. 5191–5198, 2021.
- [19] K. M. Judd and J. D. Gammell, “Multimotion visual odometry,” *The International Journal of Robotics Research*, vol. 43, no. 8, pp. 1250–1278, 2024.
- [20] J. Morris, Y. Wang, M. Kliniewski, and V. Ila, “Dynosam: Open-source smoothing and mapping framework for dynamic slam,” *IEEE Transactions on Robotics*, 2025.
- [21] R. A. Newcombe, D. Fox, and S. M. Seitz, “Dynamicfusion: Reconstruction and tracking of non-rigid scenes in real-time,” in *IEEE Conference on Computer Vision and Pattern Recognition (CVPR)*, 2015, pp. 343–352.
- [22] J. R. Lamarca, S. Parashar, J. M. M. Montiel, and A. Bartoli, “Defslam: Tracking and mapping of deforming scenes from monocular sequences,” *IEEE Transactions on Robotics*, vol. 36, no. 4, pp. 1046–1061, 2020.
- [23] C. Tang, S. Zhu, and I. Suh, “Nr-slam: Real-time non-rigid slam with neural implicit representation,” in *IEEE/RSJ International Conference on Intelligent Robots and Systems (IROS)*, 2022, pp. 1–8.
- [24] L. Heng, S. Leutenegger, and M. Pollefeys, “Semi-direct visual odometry for aided inertial navigation,” in *IEEE/RSJ International Conference on Intelligent Robots and Systems (IROS)*, 2015, pp. 3997–4004.
- [25] Z. Yang, P. Geneva, K. Eickenhoff, and G. Huang, “Degeneracy analysis for visual-inertial navigation,” *IEEE Transactions on Robotics*, vol. 34, no. 6, pp. 1622–1640, 2018.
- [26] C. Forster, L. Carlone, F. Dellaert, and D. Scaramuzza, “On-manifold preintegration for real-time visual-inertial odometry,” *IEEE Transactions on Robotics*, vol. 33, no. 1, pp. 1–21, 2017.
- [27] S. Cerezo and J. Civera, “Gnss-inertial state initialization using interepoch baseline residuals,” *IEEE Robotics and Automation Letters*, vol. 11, no. 2, pp. 1458–1465, 2026.
- [28] H. Alismail, B. Browning, and S. Lucey, “Photometric bundle adjustment for vision-based slam,” in *Asian Conference on Computer Vision*. Springer, 2016, pp. 324–341.
- [29] J. J. G. Rodríguez, J. M. M. Montiel, and J. D. Tardós, “Nr-slam: Non-rigid monocular slam,” *IEEE Transactions on Robotics*, vol. 40, no. 5, pp. 3997–4016, 2024, earlier version: arXiv:2308.04036.
- [30] J. J. Gómez-Rodríguez, J. Lamarca, J. Morlana, J. D. Tardós, and J. M. Montiel, “Sd-defslam: Semi-direct monocular slam for deformable and intracorporeal scenes,” in *2021 IEEE international conference on robotics and automation (ICRA)*. IEEE, 2021, pp. 5170–5177.
- [31] J. A. Hesch, D. G. Kottas, S. L. Bowman, and S. I. Roumeliotis, “Consistency analysis and improvement of vision-aided inertial navigation,” *IEEE Transactions on Robotics*, vol. 30, no. 1, pp. 158–176, 2014.
- [32] D. Recasens Lafuente, M. R. Oswald, M. Pollefeys, and J. Civera, “The drunkard’s odometry: Estimating camera motion in deforming scenes,” *Advances in Neural Information Processing Systems*, vol. 36, 2024.